ACCSCIENCE PUBLISHING

Journal of Seismic Exploration

ARTICLE

Full waveform inversion for a long-wavelength velocity model using a regenerated wavefield based on the SWEET method

Seoje Jeong[1], Sumin Kim[2], Woohyun Son[3], and Wookeen Chung[2]*

[1]Department of Convergence Study on the Ocean Science and Technology, Ocean Science and Technology School, National Korea Maritime & Ocean University, Busan, Republic of Korea

[2]Department of Energy and Resources Engineering, National Korea Maritime & Ocean University, Busan, Republic of Korea

[3]Marine Geology and Energy Division, Korea Institute of Geoscience and Mineral Resources, Daejeon, Republic of Korea

Abstract

In full waveform inversion (FWI), long-wavelength velocity models are essential for accurately estimating subsurface physical parameters. However, building long-wavelength velocity models with low-frequency components is challenging due to mechanical limitations in seismic data acquisition. We propose a novel FWI method that utilizes a regenerated wavefield derived from the Suppressed Wave Equation Estimation of Traveltime (SWEET) algorithm. The regenerated wavefield in our approach was obtained by convolving the arbitrary source wavelet with a Green's function, which is represented by the first-arrival traveltime and amplitude extracted from the SWEET algorithm. Our approach can build long-wavelength velocity models, provided that a low-frequency wavelet is used. Furthermore, the potential for multi-scale inversion was demonstrated by gradually increasing the frequency of the source wavelet, leading to the acquisition of high-resolution models. In numerical examples, our proposed algorithm was validated using both synthetic and field data sets. We also assessed the noise sensitivity of the proposed method, confirming its applicability in practical scenarios. These results demonstrate that the proposed method is a robust and versatile tool for constructing long-wavelength and high-resolution velocity models from band-limited seismic data.

Keywords: Full waveform inversion; Long-wavelength velocity model; SWEET method; Regenerated wavefield; Multi-scale inversion

***Corresponding author:**
Wookeen Chung
(wkchung@kmou.ac.kr)

Citation: Jeong S, Kim S, Son W, Chung W. Full waveform inversion for a long-wavelength velocity model using a regenerated wavefield based on the SWEET method. *J Seismic Explor*. 2025;34(6):78-96.
doi: 10.36922/JSE025370071

Received: September 11, 2025

Revised: November 3, 2025

Accepted: November 10, 2025

Published online: December 2, 2025

1. Introduction

Full waveform inversion (FWI) estimates subsurface physical parameters by minimizing the misfit between observed and modeled seismic data.[1-3] However, successful FWI requires addressing nonlinearity, substantial computational demands, and dependence on an appropriate initial velocity model.[4-6] In particular, a reliable initial velocity is essential for avoiding cycle skipping and for robust convergence when applying FWI to field data.[7] One approach to improving the accuracy of the initial velocity model is to build long-wavelength velocity models and use them as the initial velocity model

for FWI. Many studies have proposed constructing long-wavelength velocity models, with first-arrival tomography being a commonly used technique,[8,9] and a reflection tomography approach[10] has typically been employed to generate initial velocity models for waveform inversion.[11-14]

Traveltime tomography has been developed to achieve progressively higher-resolution models starting from long-wavelength models. This method, which relies on ray-tracing theory and the high-frequency approximation, is less sensitive to the initial velocity model.[15,16] However, conventional traveltime tomography often falls short of the resolution requirements for FWI because it does not utilize phase and amplitude information.[17,18] Using the phase and traveltime of the first-arrival wavefield, Liu et al.[19] proposed the first-arrival phase-traveltime tomography (FPT). Nevertheless, FPT has a drawback in that it does not consider the amplitude of the first-arrival wavefield, making it difficult to accurately generate detailed structures.

Another approach involves transforming the observed and modeled seismic data to reconstruct the wavefield by utilizing specific waveform attributes, such as instantaneous phase, envelope, and Laplace-transformed data. For example, Shin and Cha[20] proposed a Laplace-domain waveform inversion to extract low-wavenumber components from high-frequency seismic data, thereby generating an initial velocity model for FWI. Although the Laplace domain, like tomography, does not consider phase information,[21] by utilizing a multi-scale inversion approach with varying damping factors during the Laplace transform, it is possible to build relatively high-resolution initial velocity models. Moreover, various studies have proposed building long-wavelength velocity models using envelope data derived through the application of the Hilbert transform. Similar to Laplace-domain waveform inversion, envelope inversion faces challenges in accurately resolving detailed subsurface structures due to the lack of phase information.[22,23] Notably, recent advancements have introduced methods that incorporate phase information during the envelope inversion process, thereby improving the resolution of the inverted models.[24] These approaches aim to overcome the lack of low-frequency components in the data used for generating long-wavelength velocity models.

Recently, several complementary strategies have been developed to improve FWI convergence. Reflection waveform inversion separates a smooth background model from short-wavelength reflectivity, allowing reflections to contribute low-wavenumber updates to the background model and thereby reducing dependence on very low frequencies in the recorded data.[25-27] In addition, low-frequency extrapolation methods, including global multi-scale deep networks, reconstruct sub-band energy from band-limited recordings.[28] In parallel, improved convexity or robust misfit functions and extended search spaces mitigate nonconvexity and reduce sensitivity to the background model.[29-31] Pretrained or self-supervised frameworks provide informative priors and warm-start initialization, which can be coupled with physics-based optimization.[32-34] Despite the progress, most long-wavelength building strategies remain limited when low frequencies are missing and when phase and amplitude along the first-arrival wavefield are not exploited.

Consequently, we introduce an approach that leverages traveltime and amplitude information extracted under high-damping conditions to reconstruct a reliable long-wavelength background model for FWI. The approach, referred to as FWI using a regenerated wavefield based on the Suppressed Wave Equation Estimation of Traveltime (SWEET) algorithm (FWI-RWS), utilizes the first-arrival traveltime and amplitude to regenerate a wavefield that contains low-frequency components. The SWEET algorithm is typically employed to derive traveltimes for refraction tomography. It uses the characteristics of the observed seismic data transformed under high-damping conditions in the Laplace domain to approximate the first-arrival time and amplitude. By integrating this method, FWI-RWS aims to enhance the accuracy of the long-wavelength velocity model and provide robust results for subsequent multi-scale FWI on field data.

To implement the proposed method, we regenerated the wavefield by convolving the first-arrival traveltimes and amplitudes obtained from each receiver with an arbitrary source wavelet. This process allows for the successful construction of long-wavelength velocity models by generating wavefields that contain low-frequency components. In addition, to effectively mitigate nonlinearity, a multi-scale method that starts the inversion at low frequencies and fits higher-frequency components sequentially was applied.[35] We demonstrated through preliminary tests that multi-scale inversion is possible depending on the frequency characteristics of the convolved source wavelet, thereby enabling the stable acquisition of long-wavelength models.

The theory and methodology of FWI with the SWEET algorithm are presented, and the effectiveness of the proposed method is demonstrated using synthetic data. We also discuss the robustness of the proposed method in noisy environments, which is a known limitation of the SWEET algorithm. Finally, field data results are presented to verify the applicability of FWI-RWS.

2. Methodology

2.1. Regenerated wavefield based on the SWEET method

In this section, the basic theory of the regenerated wavefield based on the SWEET method is reviewed. In the time domain, a wavefield u can be approximated as a series of spikes.[36]

$$u(t)=\sum_{q}A_{q}\delta\left(t-t_{q}\right) \tag{I}$$

where A_q and t_q represent the amplitude and q-th time step (counted from the first-arrival event), respectively, and δ is the Dirac delta function. By multiplying **Equation (I)** by an exponential damping factor e^{-st} and integrating it, the wavefield $\tilde{u}$ in the Laplace domain can be written as follows:[36,37]

$$\tilde{u}(s)=\int_{0}^{\infty}u(t)e^{-st}dt\approx A_{f}e^{-st_{f}} \tag{II}$$

where s is a positive real number known as the Laplace damping constant, t_f is the first-arrival traveltime, and A_f is the amplitude at the first-arrival traveltime. By taking the derivative of **Equation (II)** with respect to s and dividing it by $\tilde{u}$, the equation becomes:

$$\frac{\partial\tilde{u}(s)}{\partial s}=-t_{f}A_{f}e^{-st_{f}}=-t_{f}\tilde{u}(s) \tag{III}$$

Therefore, the first-arrival traveltime and amplitude are defined as follows:

$$t_{f}=-\frac{1}{\tilde{u}(s)}\frac{\partial\tilde{u}(s)}{\partial s} \tag{IV}$$

and

$$A_{f}=\tilde{u}(s)e^{st_{f}} \tag{V}$$

In this study, the wavefield in the time domain was regenerated by convolving the traveltime and amplitude, calculated from **Equations (IV)** and **(V)**, with an arbitrary source wavelet.

The regenerated wavefield $\bar{u}$ is given by:

$$\bar{u}(t)=w(t)*\left[A_{f}\delta\left(t-t_{f}\right)\right] \tag{VI}$$

where w is the source wavelet, and $*$ is the convolution operator.

2.2. FWI using a regenerated wavefield based on the SWEET method (FWI-RWS)

In its classical formulation, FWI is defined as an optimization problem that seeks to minimize an objective function, and FWI-RWS has a similar form to FWI. The objective function E, based on the l_2-norm of residuals between the observed and modeled data, can be expressed as[2]:

$$E=\frac{1}{2}\sum_{i}^{N_s}\sum_{j}^{N_r}\left\|\bar{u}_{i,j}-\bar{d}_{i,j}\right\|_{2}^{2} \tag{VII}$$

where $\|\ldots\|_2^2$ is the l_2-norm, $\bar{u}_{i,j}$ and $\bar{d}_{i,j}$ are the regenerated traces both for modeled and observed traces using **Equation (VI)**, i and j indicating the source and the receiver locations, and N_s and N_r are the number of sources and receivers, respectively. The gradient with respect to the k-th subsurface model parameter m_k can be expressed as:

$$\nabla E=\frac{\partial E}{\partial m_{k}}=\sum_{i}^{N_s}\sum_{j}^{N_r}\left(\frac{\partial\bar{u}_{i,j}}{\partial m_{k}}\right)^{T}\cdot\bar{r}_{i,j} \tag{VIII}$$

where $\frac{\partial\bar{u}_{i,j}}{\partial m_k}$ is the partial derivative wavefield using the regenerated wavefield, $\bar{r}_{i,j}$ is the data residual calculated by $\bar{u}_{i,j}-\bar{d}_{i,j}$, T is transpose, and $\cdot$ is the dot product operator.

In conventional FWI, as calculating **Equation (VIII)** leads to substantial computational cost, the adjoint-state method is used to reduce the computational burden associated with the partial derivative wavefield.[38] Similarly, we aim to apply the adjoint-state method to the proposed approach. By substituting **Equation (VI)** into **Equation (VIII)**, the partial derivative wavefield can be expressed as follows:

$$\begin{aligned}\frac{\partial\bar{u}_{i,j}}{\partial m_{k}}&\approx\frac{\bar{u}_{i,j}\left(m_{k}+\Delta m\right)-\bar{u}_{i,j}\left(m_{k}\right)}{\Delta m}\\&=w_{i}(t)*\left(\frac{A_{f}^{p}-A_{f}^{b}}{\Delta m}\right)\delta\left(t-t_{f}\right)\\&=w_{i}(t)*\left(\frac{A_{f}^{p}-A_{f}^{b}}{\Delta m}\right)\delta\left(t-t_{f}\right)\end{aligned} \tag{IX}$$

with

$$\bar{u}_{i,j}\left(m_{k}+\Delta m\right)=w_{i}(t)*\left[A_{f}^{p}\delta\left(t-t_{f}\right)\right] \tag{X}$$

$$\bar{u}_{i,j}\left(m_{k}\right)=w_{i}(t)*\left[A_{f}^{b}\delta\left(t-t_{f}\right)\right] \tag{XI}$$

where f_i is the source wavelet, indicating the use of the i-th source wavelet. In **Equation (IX)**, the first-arrival traveltime t_f remains the same regardless of Δm, while A_f^p and A_f^b denote the first-arrival amplitudes computed from the perturbed model $m_k+\Delta m$ and background model m_k, respectively. Therefore, the partial derivative wavefield can be further simplified as follows:

$$\Delta A_f = A_f^p - A_f^b \frac{\partial \overline{\mathrm{u}}_{i,j}}{\partial m_k} = w_i(t) * \frac{\Delta A_f}{\Delta m}\delta(t-t_f) = \left(\frac{\mathrm{u}_{i,j}(m_k+\Delta m)-\mathrm{u}_{i,j}(m_k)}{\Delta m}\right) = \left(\overline{\frac{\partial \mathrm{u}_{i,j}}{\partial m_k}}\right) \quad \text{(XII)}$$

Through **Equations (VIII), (IX),** and **(XII),** we can confirm that applying **Equation (VI)** to the partial derivative wavefield yields results identical to the regenerated wavefield. To verify **Equation (XII),** we used a homogeneous velocity model of 1.5 km/s on a 201 × 101 grid (Figure 1A). The grid size was 10 m and the time interval was 1 ms. Figure 1A shows a single shot at 800 m and a single receiver at 1,200 m, both positioned on the surface. The point-scatterer was located at (1,000 m, 500 m) at the center of the velocity model. The source signature was a Ricker wavelet with a dominant frequency of 5 Hz. The partial derivative wavefield at the point-scatterer within a simple subsurface model was compared with results obtained from numerical differentiation. In Figure 1B, the comparison of the results from convolving the same sources with **Equation (XII)** indicates excellent agreement between the two approaches.

To reduce the computational burden of FWI-RWS, the adjoint-state method was applied. The partial derivative wavefield for the regenerated wavefield in **Equation (VIII)** can be expressed as follows:

$$\frac{\partial \overline{\mathrm{u}}_{i,j}}{\partial m_k} = \left(\overline{\frac{\partial \mathrm{u}_{i,j}}{\partial m_k}}\right) = \mathrm{G} * \overline{\mathrm{v}}_{i,j} \quad \text{(XIII)}$$

where G is Green's operator, $\overline{\frac{\partial \mathrm{u}_{i,j}}{\partial m_k}}$ is the regenerated partial derivative wavefield, and $\overline{\mathrm{v}}_{i,j}$ is the regenerated virtual source wavefield. To verify **Equation (XIII),** the gradient to a perturbation point within the subsurface model (Figure 1A) was examined. This yielded two distinct gradient estimates: one calculated using the finite-difference method and the other obtained using the virtual source. Figure 2 shows that the two gradients closely match. By substituting **Equation (XIII)** into **Equation (VIII),** the gradient using the regenerated wavefield can be expressed as follows:

$$\begin{aligned}
&\nabla E = \\
&\sum_i^{N_s}\sum_j^{N_r}\int_0^{\mathrm{T_{max}}}\left(\frac{\partial \overline{u}_{i,j}(t)}{\partial m_k}\right)\Delta \overline{r}_{i,j}(t)dt = \sum_i^{N_s}\sum_j^{N_r}\left(\frac{\partial \overline{u}_{i,j}(t)}{\partial m_k}\right)\otimes \overline{r}_{i,j}(t) \\
&= \sum_i^{N_s}\sum_j^{N_r}\left[G(t) * \overline{v}_{i,j}(t)\right]\otimes \overline{r}_{i,j}(t) = \sum_i^{N_s}\sum_j^{N_r}\overline{v}_{i,j}(t) \\
&*\left[G(t) * \overline{r}_{i,j}(\mathrm{T_{max}}-t)\right] \\
&= \sum_i^{N_s}\sum_j^{N_r}\overline{v}_{i,j}(t) * B_{i,j}(t) = \sum_i^{N_s}\sum_j^{N_r}\overline{v}_{i,j}(t)\otimes B_{i,j}(\mathrm{T_{max}}-t) \\
&= \sum_i^{N_s}\sum_j^{N_r}\int_0^{\mathrm{T_{max}}}\overline{v}_{i,j}(t)B_{i,j}(\mathrm{T_{max}}-t)dt \text{ with } B_{i,j} \\
&(t) = G(t) * \overline{r}_{i,j}(\mathrm{T_{max}}-t)
\end{aligned} \quad \text{(XIV)}$$

where $B_{i,j}$ is the backpropagated wavefield with the regenerated residual wavefield, and ⊗ denotes the zero-lag cross-correlation.

Based on the steepest-descent method, the model update at each iteration is expressed as[38]:

$$\mathrm{m}^{l+1} = \mathrm{m}^l - \alpha \times \Delta \mathrm{m} \quad \text{(XV)}$$

where m^l is the subsurface model parameter for l-th iteration, α is the step length, and Δm is the update direction.

In this study, the diagonal term of a pseudo-Hessian was used as a preconditioner for the gradient[21]. Furthermore, to mitigate model dependence in seismic imaging, a multi-scale strategy was employed, applying the FWI method across a spectrum of frequencies, progressing from low-frequency to high-frequency components.[39] The conventional multi-scale FWI approach enhances resolution by progressively incorporating the low-frequency to high-frequency components of the observed data.[1-3] Overall, a multi-scale FWI-RWS approach was introduced by gradually increasing the maximum frequency of the source wavelet used in **Equation (VI)**. Figure 3 shows the workflow of multi-scale FWI-RWS, which can be divided into eight steps:

(i) Set initial velocity model parameters and source wavelet for low frequencies.
(ii) Perform forward propagation modeling.
(iii) Extract the traveltime and amplitude of the shot gathers.
(iv) Convolve the arbitrary source wavelet with the extracted traveltime and amplitude to regenerate the wavefield.
(v) Use the calculated regenerated wavefield, virtual source, and residual to perform backward propagation modeling.

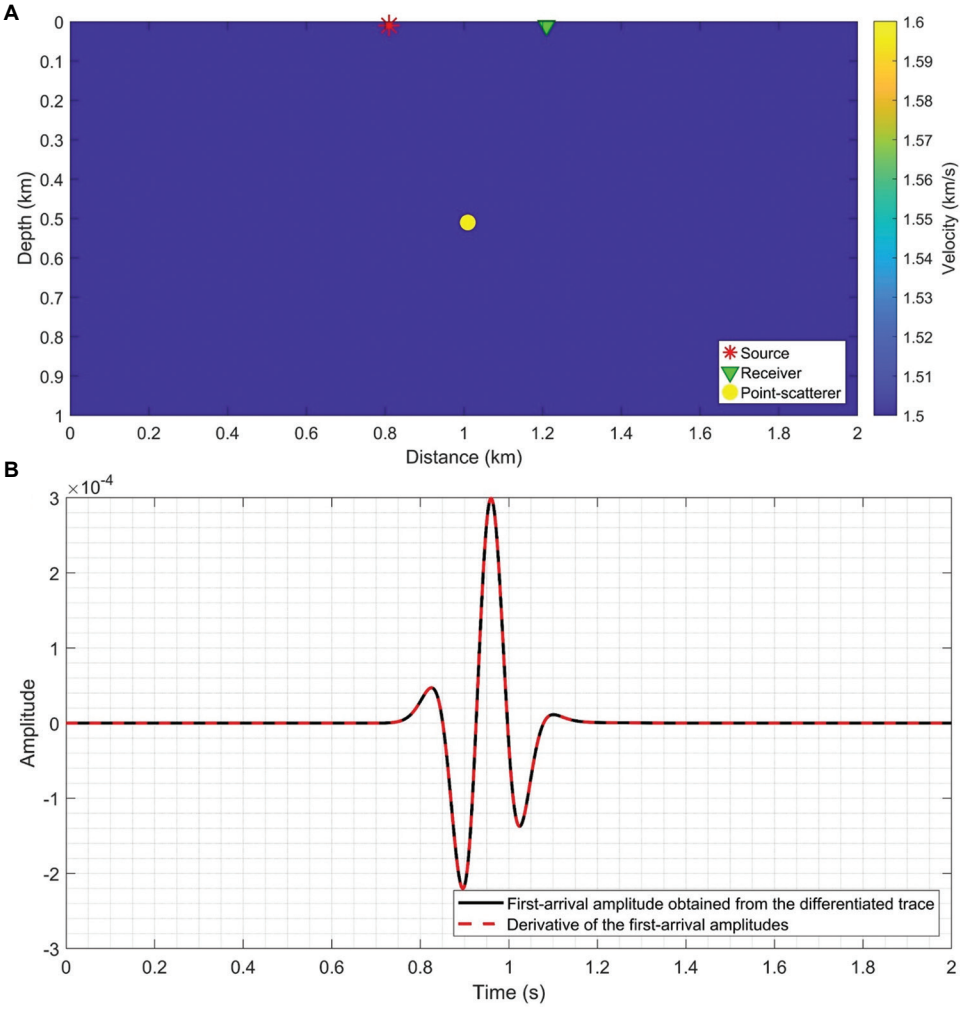

Figure 1. Geometry of the homogeneous model and validation of **Equation [XII].** (A) The homogeneous velocity model illustrates the source, receiver, and point-scatterer locations. (B) Comparison of results obtained by convolving the same source wavelet with the first-arrival amplitude obtained from the differentiated trace (solid black line) and the derivative of the first-arrival amplitudes from the point-scatterer and background models (dashed red line).

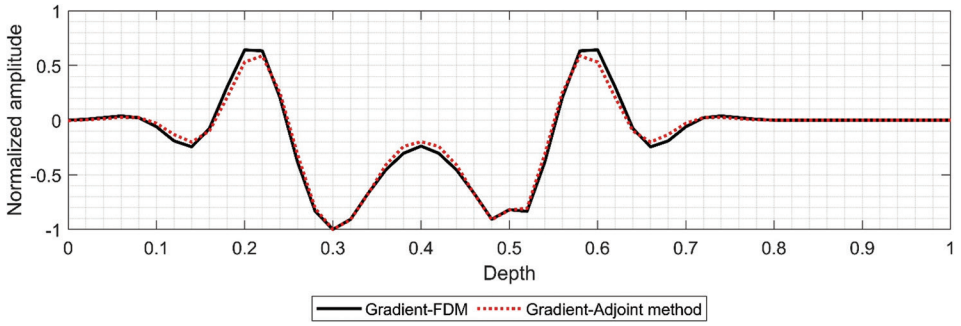

Figure 2. A comparison of the gradient between the finite-difference method (**Equation [IX]**; solid black line) and the adjoint formulation (**Equation [XIII]**; dashed red line)
Abbreviation: FDM: Finite-difference method.

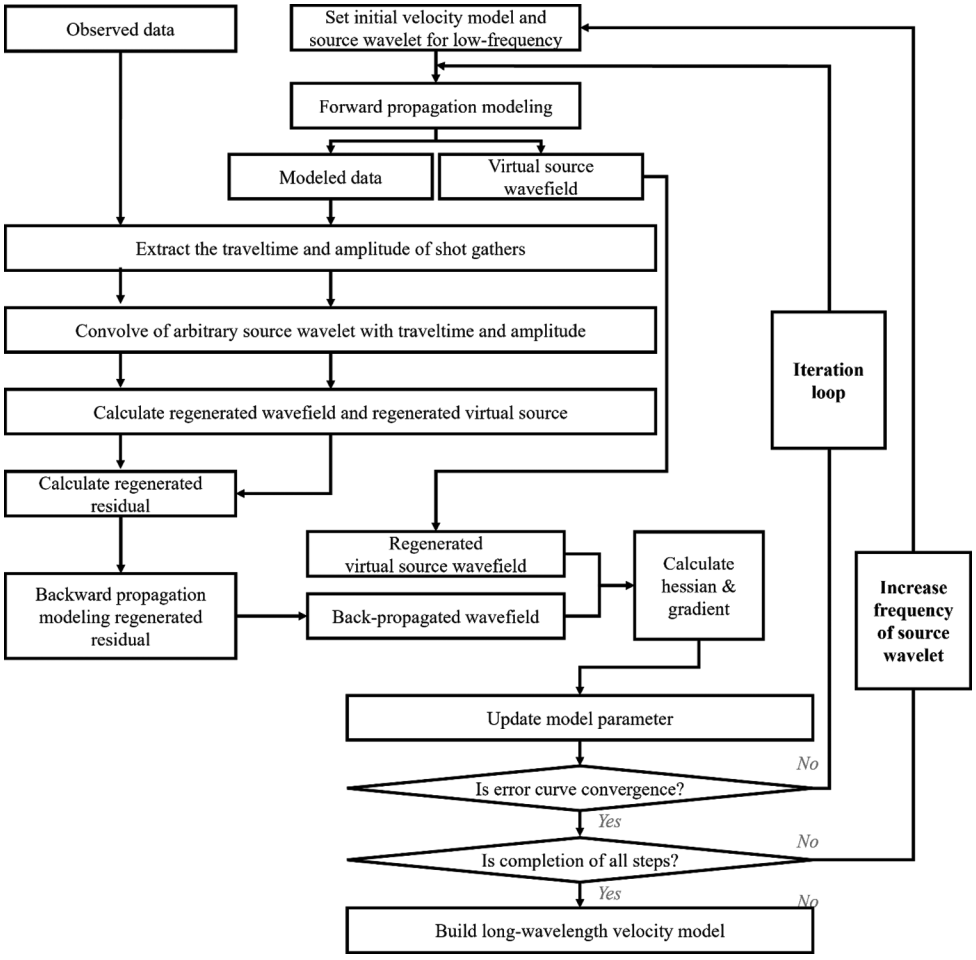

Figure 3. Workflows of multi-scale FWI-RWS

(vi) Update the velocity model using the regenerated wavefield.
(vii) Check the error curve convergence and increase the frequency of the source wavelet.
(viii) Build a long-wavelength velocity model.

3. Results

3.1. Analysis of the regenerated wavefield and gradient using a three-layer velocity model

In the numerical tests, we solved the 2D isotropic, constant-density acoustic wave equation in the time domain. The propagator employed second-order central differences in space and a second-order three-level time scheme. To analyze how the maximum frequency of the arbitrary source wavelet in **Equation (VI)** affects the shot gathers and the corresponding gradients, we designed a synthetic experiment using a three-layer model (Figure 4). The initial velocity model was homogeneous with a velocity of 1.5 km/s. The top boundary was treated as a free surface boundary, while the remaining sides employed convolutional perfectly matched layers.[40] The model grid comprised 601 × 201 points with 10.0 m spacing in both directions. The time sampling interval was 1 ms, and the recording length was 5.0 s. A total of 57 shots were deployed from x = 0.2 to x = 5.8 km at 100 m spacing. For each shot, 601 receivers were distributed along the velocity model surface, with a receiver interval of 10 m. The source signature was a Ricker wavelet with a dominant frequency of 5 Hz. Shot gathers were generated by propagating wavefields induced by the arbitrary source wavelet and subsequently used to compute and analyze the gradients within the multi-scale FWI-RWS workflow.

Figure 5A-C shows the modeled data, observed data, and residuals obtained by forward modeling. Figure 5D-L illustrates the regenerated modeled data, observed data, and residuals after convolution with Ricker wavelets at three different maximum frequencies: 15 Hz (Figure 5D-F), 1 Hz (Figure 5G-I), and 0.5 Hz (Figure 5J-L). As frequency decreased, the observed and modeled data became smoother, and the residuals grew broader and less detailed.

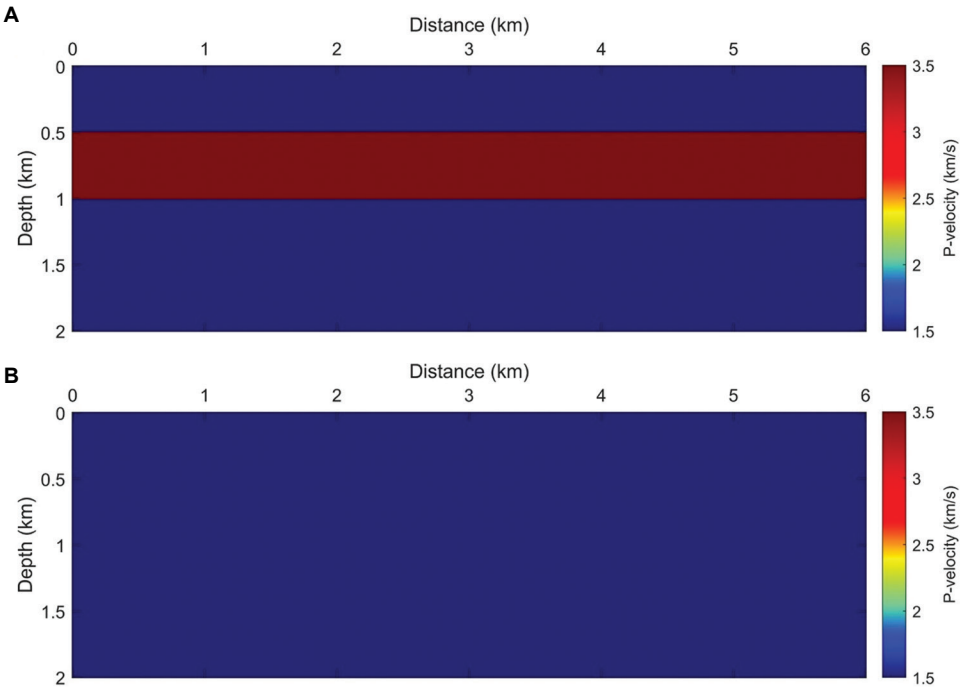

Figure 4. Test velocity models. (A) The three-layer velocity model. (B) The initial velocity model.

Based on **Equations (IV)** and **(V)**, the first-arrival traveltime and amplitude of the wavefield, as shown in Figure 6, were obtained with a Laplace damping constant of 15. As the maximum frequency of the convolved source decreased, the regenerated wavefield contained more low-frequency information.

In FWI-RWS, the gradient was calculated by regenerating the virtual source and the backward-propagated wavefields. To compare the inversion capabilities of conventional FWI and FWI-RWS on the three-layer model, we examined gradients at various frequencies: the gradient of FWI (Figure 7A) and the gradient of FWI-RWS using maximum frequencies of 15 Hz (Figure 7B), 1 Hz (Figure 7C), and 0.5 Hz (Figure 7D). The gradient of conventional FWI significantly updated the upper part of the high-velocity layer. In contrast, FWI-RWS, utilizing arbitrary source wavelets at low frequencies, updated the lower and internal parts of the high-velocity layer.

3.2. FWI-RWS using the SEG/EAGE salt model

The FWI-RWS was tested using a 2D section of the Society of Exploration Geophysicists/European Association of Geoscientists and Engineers (SEG/EAGE) salt model.[41] The model size was 676 × 210 points with 10.0 m spacing (Figure 8A). The synthetic dataset consisted of 186 shots, with a shot interval of 400 m. For each shot, 676 receivers were distributed along the velocity model surface, with a receiver interval of 10 m. The data recording time was 5.0 s, with a time interval of 1.0 ms. The source signature was a Ricker wavelet with a dominant frequency of 5 Hz. The initial velocity model was a linear model, with a velocity range of 1.5 km/s at the surface to 2.5 km/s at the bottom, as shown in Figure 8B. The FWI-RWS algorithm used a Laplace damping constant of 15 to extract first-arrival traveltime and amplitude.

In this case, the multi-scale FWI-RWS was performed in three steps to update the velocity model, where each step involved repeating the process across a specified frequency band. It progressively increased the maximum frequency of the source wavelet used in **Equation (VI)** from 0.05 Hz to 1 Hz, with a frequency interval of 0.05 Hz. Figure 8C shows the inverted velocity model for the 103rd iteration. The FWI-RWS results enabled the updating of broad regions of the salt body and the acquisition of a more reliable initial velocity model. When the iteration termination ε is satisfied:

$$\varepsilon < \frac{E^{l} - E^{l-1}}{E^{1}} \tag{XVI}$$

where E^{l} represents the evaluated objective function at the l-th iteration. In our test, we set ε to 0.02. The updated images for FWI-RWS from these inversion results (Figure 8C) demonstrated the potential of a multi-scale strategy. The inversion quality improved by iteratively processing the inversion from low to high frequencies of the source. Then, multi-scale FWI-RWS was used to improve

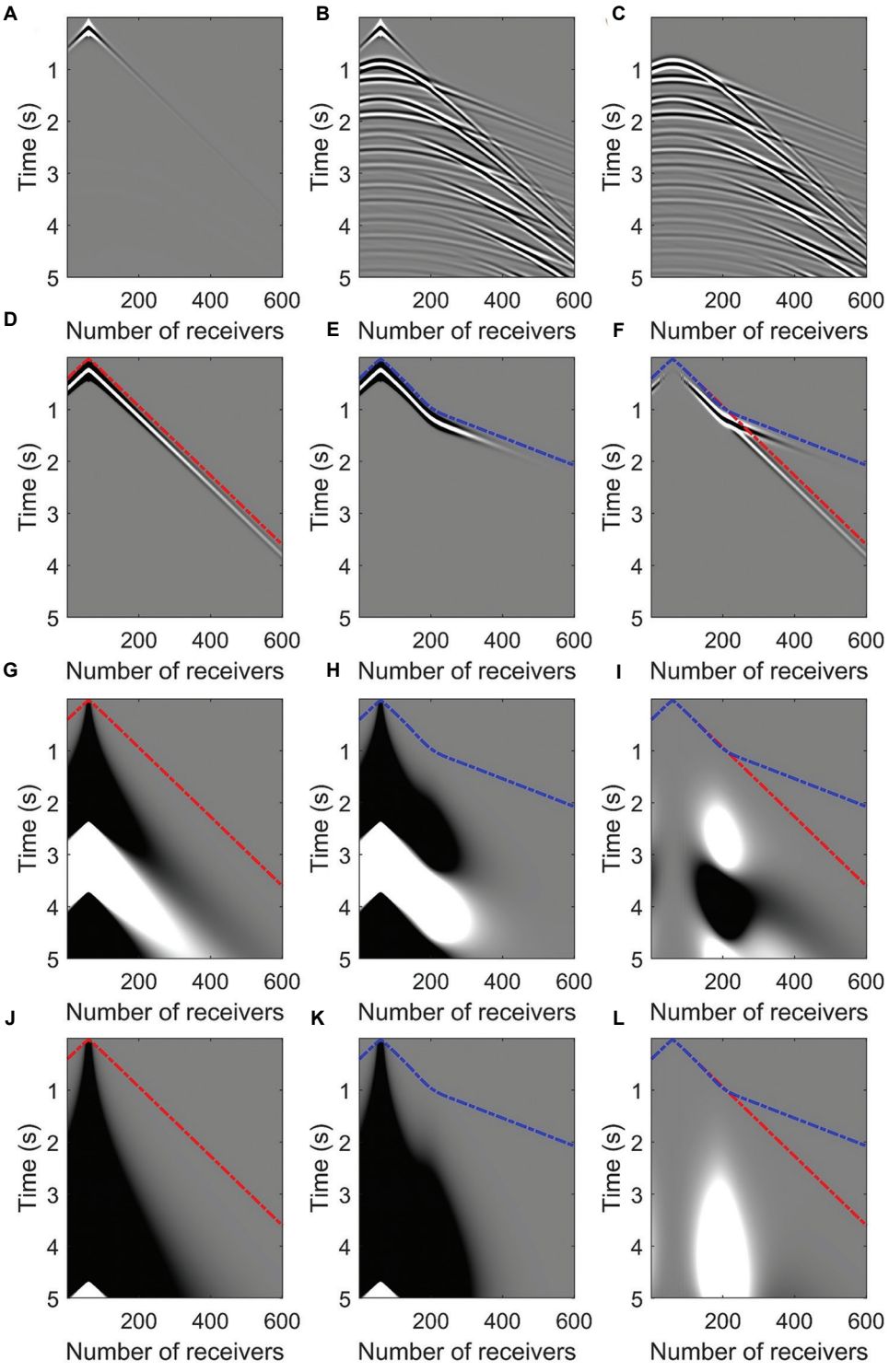

Figure 5. Comparison of the modeled data, observed data, and residuals. (A–C) Original wavefield. Regenerated wavefield using a maximum frequency of (D–F) 15 Hz, (G–I) 1 Hz, and (J–L) 0.5 Hz. The red dashed lines denote the first-arrival traveltime of the modeled data, and the blue dashed lines denote the first-arrival traveltime of the observed data.

the resolution of inverted salt structures. To evaluate the dependency of FWI results on the initial velocity model, FWI results obtained using a linear velocity model (Figure 8B) were compared with those obtained using the

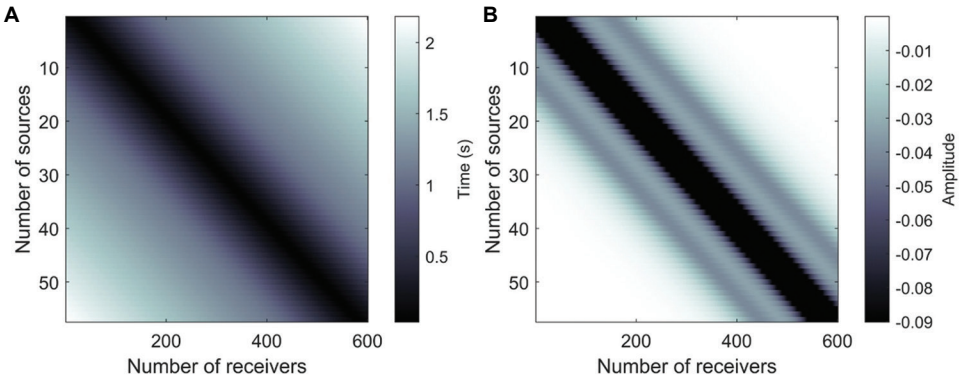

Figure 6. Spatial patterns of first-arrival traveltime and amplitude across sources and receivers. (A) First-arrival traveltime, and (B) amplitude.

FWI-RWS results (Figure 8C). The model parameters used for modeling and FWI were the same as those used in the previous example.

After 200 iterations, the FWI results using the linear velocity model as the initial velocity model only recovered the shallow part of the salt due to a lack of low-frequency information (Figure 9A). It is difficult to obtain the reflection information of the salt bottom and subsalt when there is insufficient low-frequency information. However, FWI using FWI-RWS results as the initial velocity model showed improvement with the same number of iterations (Figure 9B), showing the effectiveness of the proposed method. The proposed method allows for estimating long-wavelength components when using low-frequency source wavelets, and, as the frequency increases, it progressively recovers finer details, such as the salt boundaries shown in Figure 9B.

The analysis of the depth–velocity profiles (Figure 10) demonstrated that the proposed algorithm not only updates the model to closely resemble the true velocity but also accurately adjusts both the boundaries and internal velocities of the high-velocity layers. Figure 11 shows the history of root mean square error (RMSE) with respect to the number of iterations to assess convergence. The RMSE values were normalized by dividing the error obtained from the first iteration by the total RMSE value. As shown in Figure 11, we noted that the RMSE of the FWI using FWI-RWS results reached 0.2 of the initial value, whereas the RMSE of the FWI using the linear velocity model reached over 0.6 compared to the initial result.

3.3. Field data test

The application of the multi-scale FWI-RWS strategy was further extended to a 2D marine profile to evaluate its robustness. The 2D active seismic dataset was acquired offshore Yeosu in the South Sea by the Korea Institute of Geoscience and Mineral Resources. Seismic data acquisition was performed using a 1,050 m streamer and an airgun source. Additional acquisition parameters are shown in Table 1.

Field seismic data were first conditioned by estimating an effective source wavelet from high-signal-to-noise ratio (SNR) early arrivals. We then applied an eighth-order, zero-phase Butterworth low-pass filter (80 Hz cutoff) to limit bandwidth and resampled the data from 0.5 ms to 0.25 ms to match the modeling grid. Finally, to stabilize the multi-scale FWI-RWS updates and to comply with the regenerated-wavefield formulation, the records were convolved with a 40 Hz dominant Ricker wavelet to achieve a controlled low-frequency target wavelet. All steps were applied consistently to all shots.

Finite-difference modeling used a 0.25 ms time step with second-order accuracy in space and time. The initial velocity model was a homogeneous model with a velocity of 1.5 km/s. The model size was 8,951 × 151 grid points with 1.25 m spacing in both directions. The towed streamer had 84 channels at a 12.5 m group interval, towed at 7 ± 1 m depth, and shots were spaced 12.5 m apart with 3 s records sampled at 1 ms.

Figure 12 presents the estimated source and the Ricker wavelets (with maximum frequencies of 1, 5, and 10 Hz) used for constructing the long-wavelength velocity model. Figure 13A showcases the results of the FWI-RWS, demonstrating the construction of a long-wavelength velocity model. To achieve this, wavefields were regenerated using arbitrary sources with maximum frequency components ranging from 1 Hz to 10 Hz, incremented at 1 Hz intervals. Then, the applicability of the proposed method to field data was evaluated by applying reverse time migration (RTM) with different initial velocity models, including a homogeneous velocity model and a model derived from the FWI-RWS method. Figure 13B and C shows migration images from RTM obtained using a homogeneous model and FWI-RWS

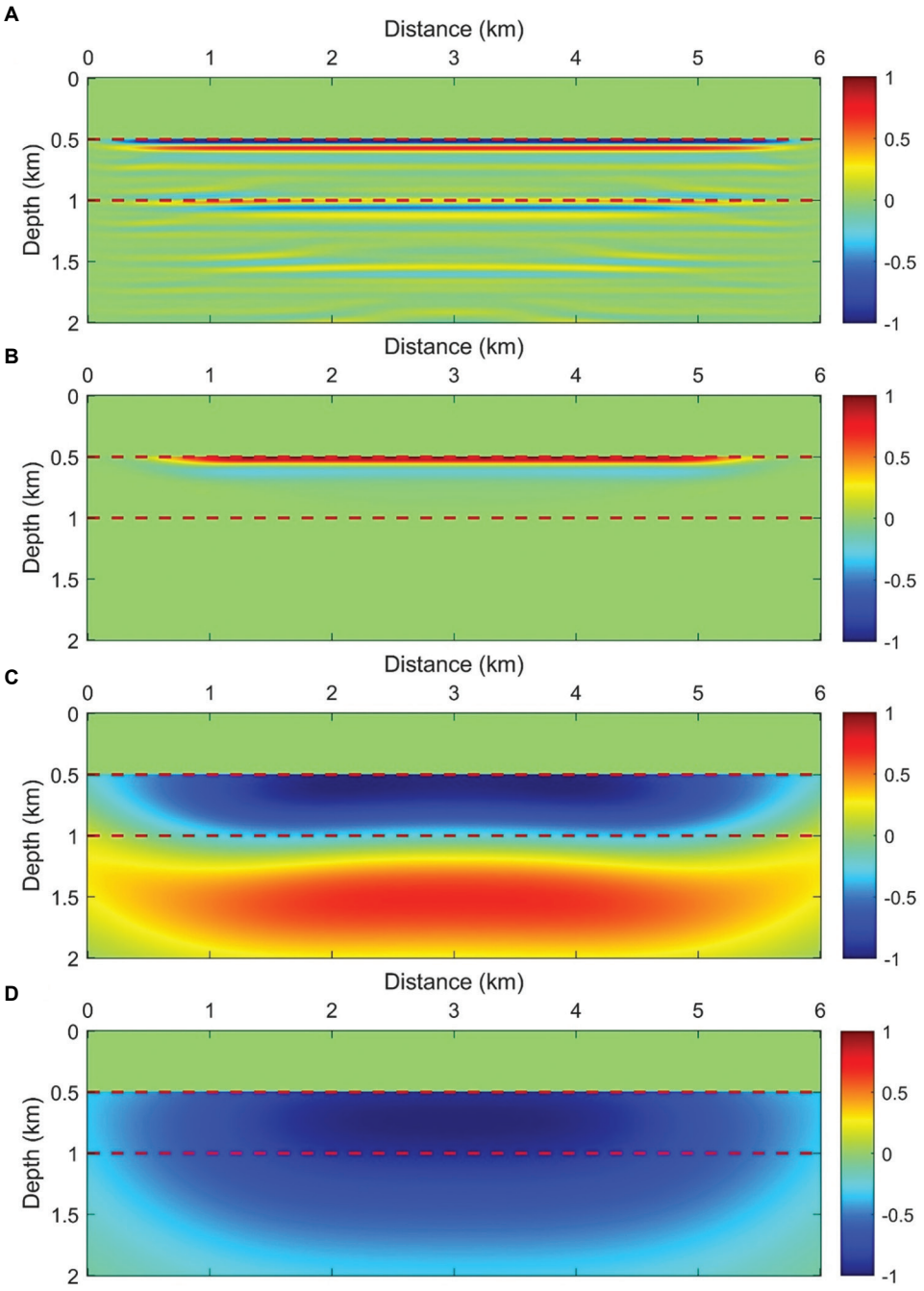

Figure 7. Gradients of (A) FWI using a maximum frequency of 15 Hz, FWI-RWS using a maximum frequency of (B) 15 Hz, (C) 1 Hz, or (D) 0.5 Hz. The red dashed lines denote the first-arrival traveltime of the modeled data, and the blue dashed lines denote the first-arrival traveltime of the observed data.

results. The RTM images generated using the FWI-RWS results (Figure 13C) showed improved amplitude balance compared to those using a homogeneous model. Compared with the RTM results using a homogeneous model, this approach also produced more accurate and high-resolution images with better continuity of subsurface structures.

For an additional analysis, the subsurface offset domain common image gather (SODCIG) obtained by RTM using the homogeneous model and the FWI-RWS results as initial velocity models were compared. Common image gathers (CIGs) are generally used as a primary criterion for validating the velocity model, with moveout guiding

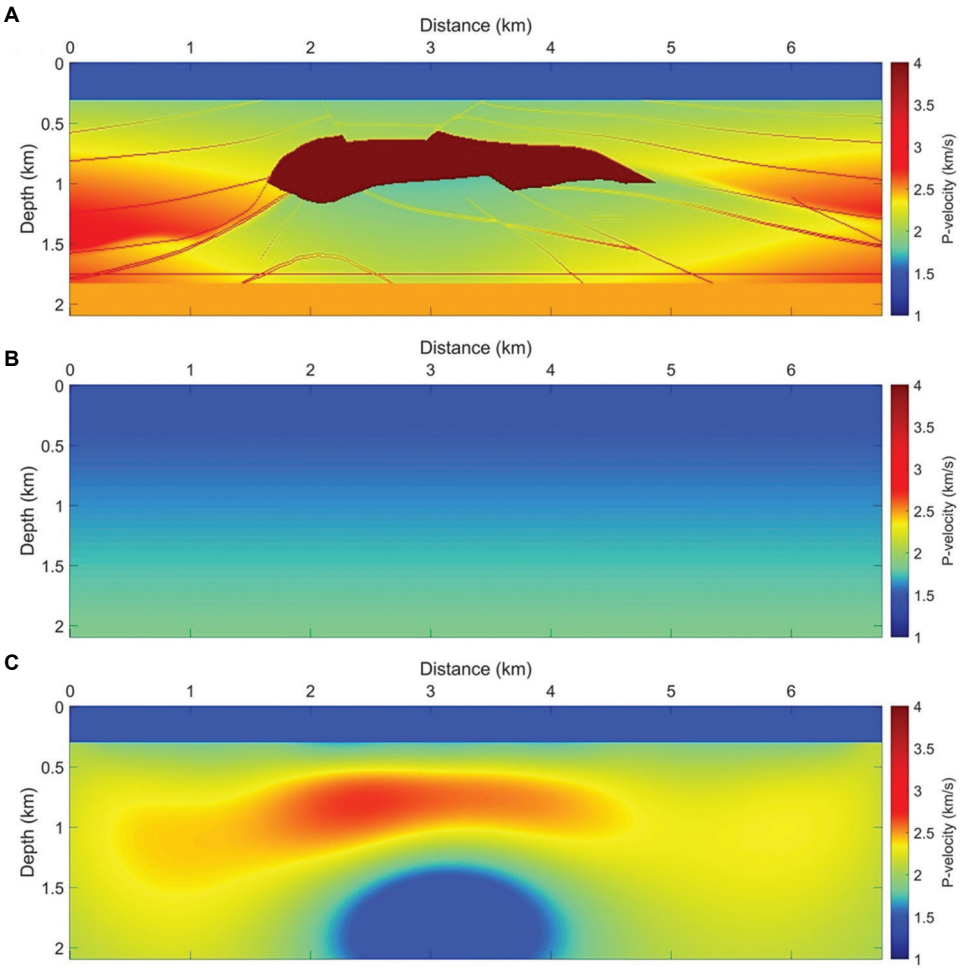

Figure 8. The 2D SEG/EAGE salt model. (A) True, (B) initial velocity model, and (C) long wavelength model of FWI-RWS results.
Abbreviation: SEG/EAGE: Society of Exploration Geophysicists/European Association of Geoscientists and Engineers.

Table 1. Seismic data acquisition parameters

Parameters	Description	Value
Streamer	Streamer length (m)	1,050
	Number of channels	84
	Group interval (m)	12.5
	Streamer depth (m)	7±1
Recording	Recording length (s)	3
	Sampling rate (ms)	1
Source	Source type	Bolt long-life air guns
	Source volume (cu. in.)	269
	Source depth (m)	5
	Source interval (m)	12.5

the velocity updates.[42-45] One type of CIG, known as the SODCIG, is characterized by accurately migrated transmitted events that are vertically aligned at zero-offset along the depth axis, while any defocusing indicates inaccuracies in the migration velocity.[46-49] Figure 14 presents SODCIGs at depths of 1, 2, and 5 km in the migration image. When using a homogeneous velocity model, most reflectors shift upward as the offset increases, indicating that the background velocity is slower than the actual velocity. In contrast, the FWI-RWS velocity model focuses the reflection energy near zero offset, though some reflectors still exhibit curvature with increasing offset. These results suggest that using the FWI-RWS model as the background velocity enhances the recovery of long-wavelength structures, leading to more accurate alignment of reflectors than using the homogeneous velocity model.

4. Discussion

When estimating the first-arrival traveltime, the Laplace transformation is sensitive to the first-arrival noise, as noted by Shin and Cha.[20] Therefore, if noise precedes the

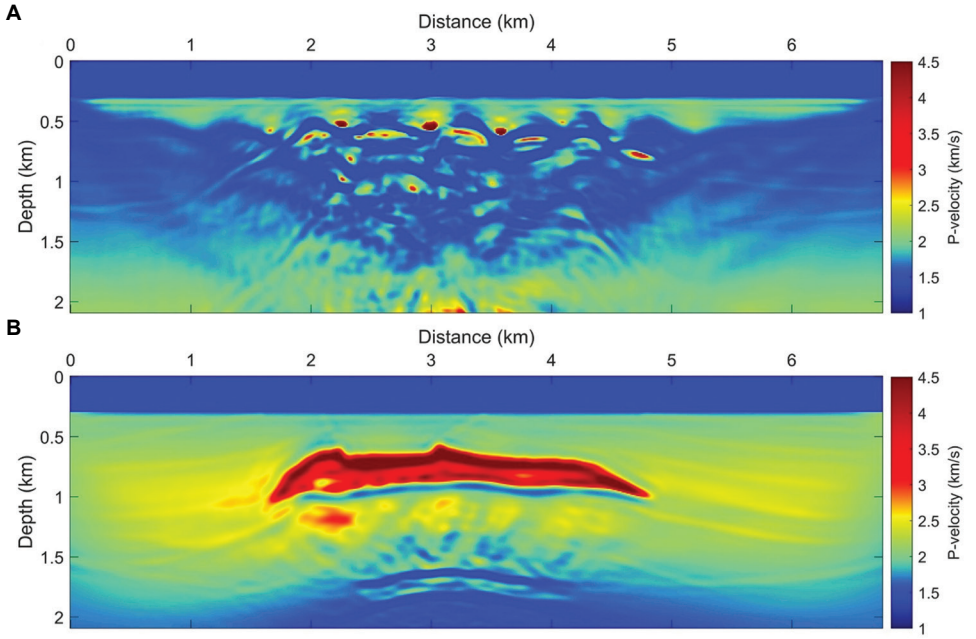

Figure 9. Full waveform inversion (FWI) results using (A) linear velocity model, and (B) FWI-RWS result as initial velocity model

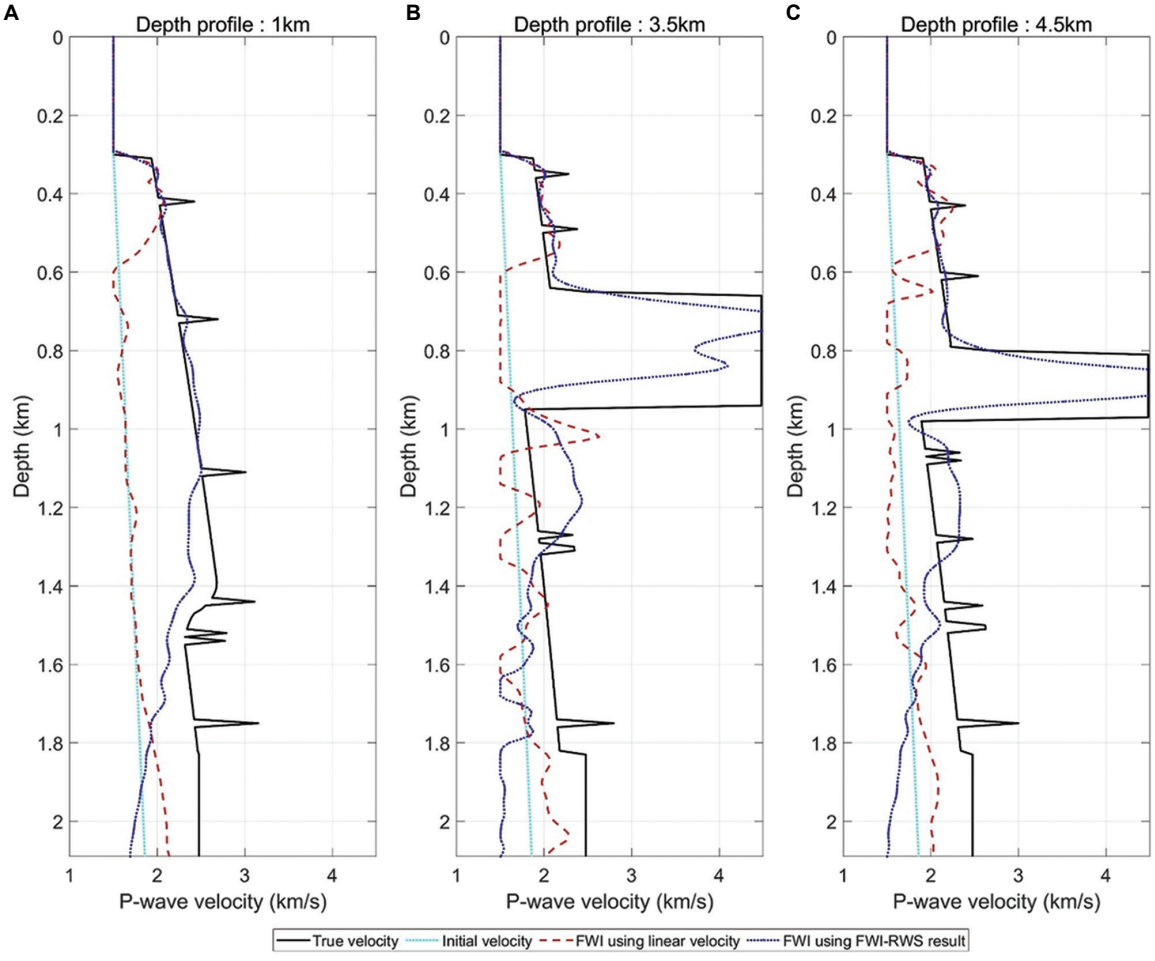

Figure 10. Comparison of depth-velocity profiles at horizontal position of (A) 1 km, (B) 3.5 km, and (C) 4.5 km. The true velocity (solid black lines), the initial velocity model (doted cyan lines), full waveform inversion (FWI) result obtained using linear velocity model (dashed red lines) and FWI-RWS result.

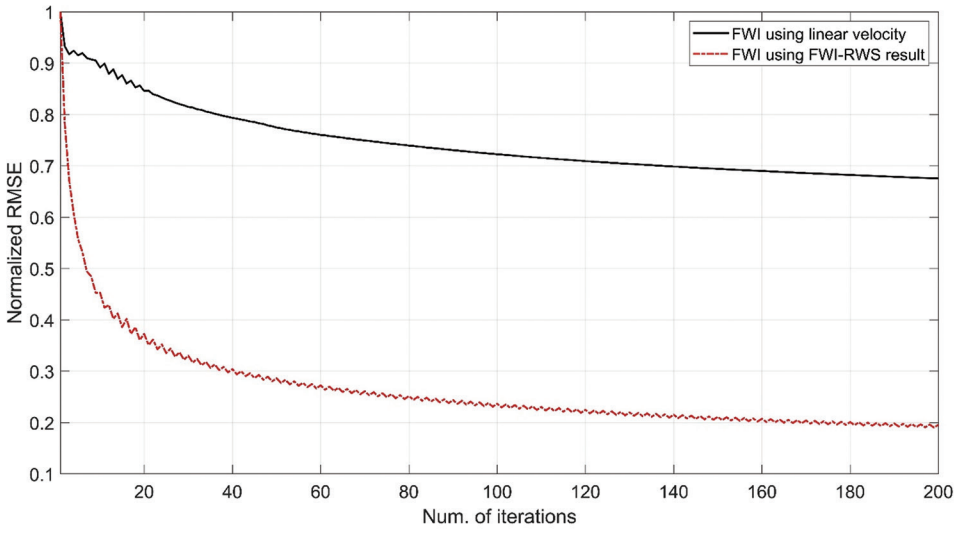

Figure 11. Root mean square error (RMSE) history of the full waveform inversion (FWI) started from the linear velocity model (solid black line) and that of the FWI started from the FWI-RWS results (dashed red line)

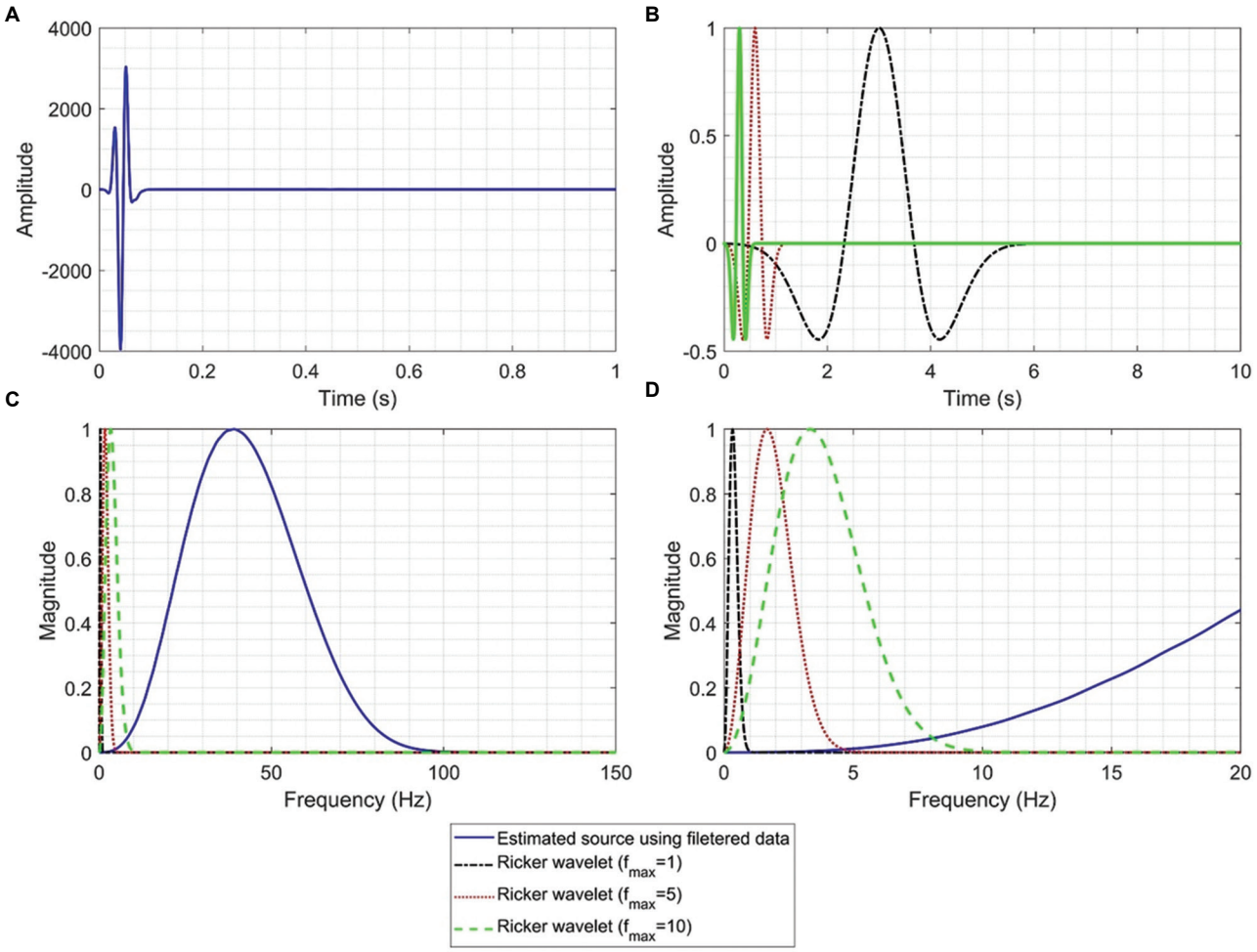

Figure 12. Estimated source analysis and band-limited convolution in time and frequency domains. (A) Estimated source using filtered data in the time domain. (B) Convolved sources with maximum frequencies of 1, 5, and 10 Hz in the time domain. (C) Frequency domain analysis of the estimated source shown in (A) and the convolved sources in (B). (D) Zoomed-in view of the frequency domain up to 20 Hz.

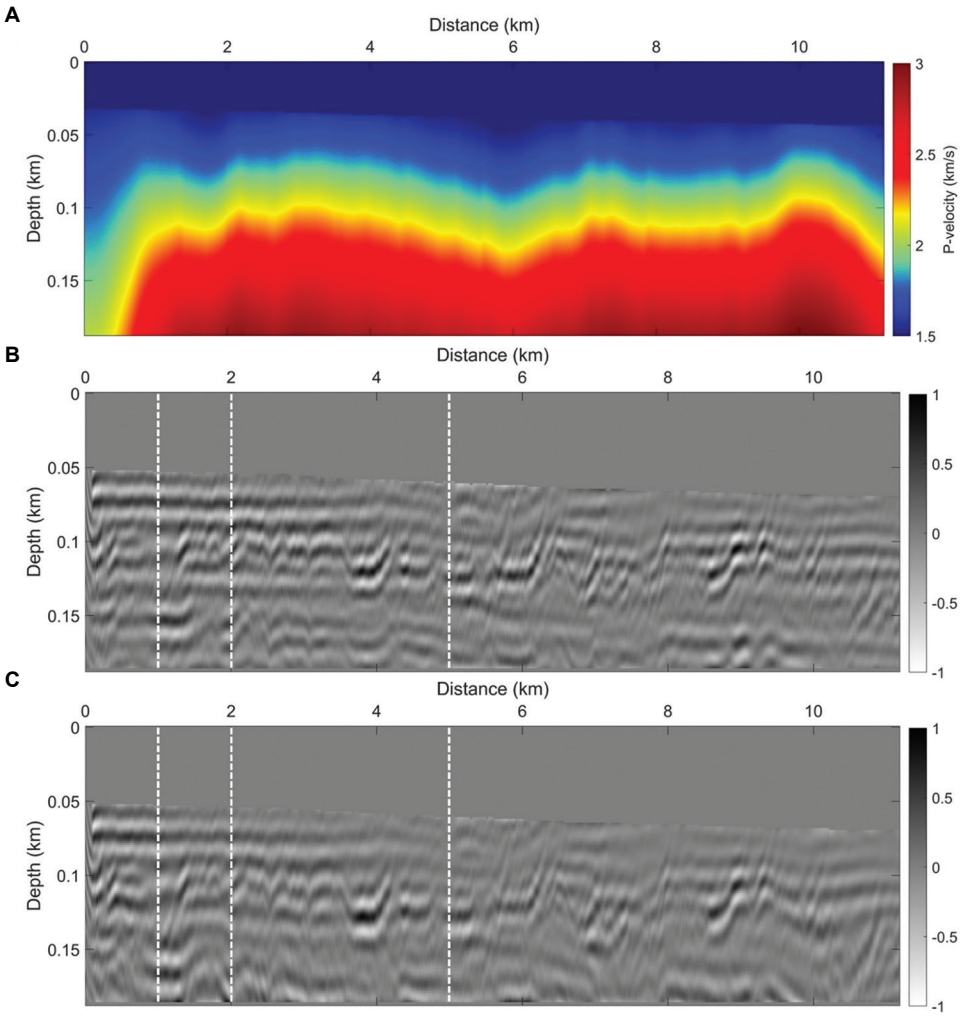

Figure 13. Imaging results from field data. (A) FWI-RWS results using field data. Reverse time migration results post-processing obtained using a (B) homogenous model, and (C) FWI-RWS results as the background velocity model.

first-arrival signal, the transform assigns it significant weight, necessitating the removal of first-arrival noise before applying the Laplace transform. To further test the applicability of the algorithm to noisy data, we analyzed the first-arrival traveltime and amplitude as a function of the SNR to assess noise sensitivity. The first-arrival traveltime and amplitude of the observed data using a strong Laplace damping factor e^{-st} are calculated as follows:

$$\tilde{d}(s)=\int_0^{\infty} d(t)e^{-st}dt \approx A_f e^{-st_f} \quad \text{(XVII)}$$

where $\bar{d}$ is the Laplace-transformed observed data.

Therefore, to analyze the noise sensitivity of the proposed method, tests were conducted with varying Laplace damping constants and intervals. For the noise test, arbitrary seismic signals were generated, and noise was added to achieve SNRs of 10 dB, 20 dB, and 30 dB (Figure 15). When the first-arrival traveltime was unknown, the error in first-arrival traveltime and amplitude increased at low SNR levels (Figure 16). The synthetic test showed results nearly identical to situations where the first-arrival traveltime was known (Figure 17). When the first-arrival traveltime was established, the process tended to yield similar outcomes, largely unaffected by the level of noise present. Successful application of this technique is anticipated if

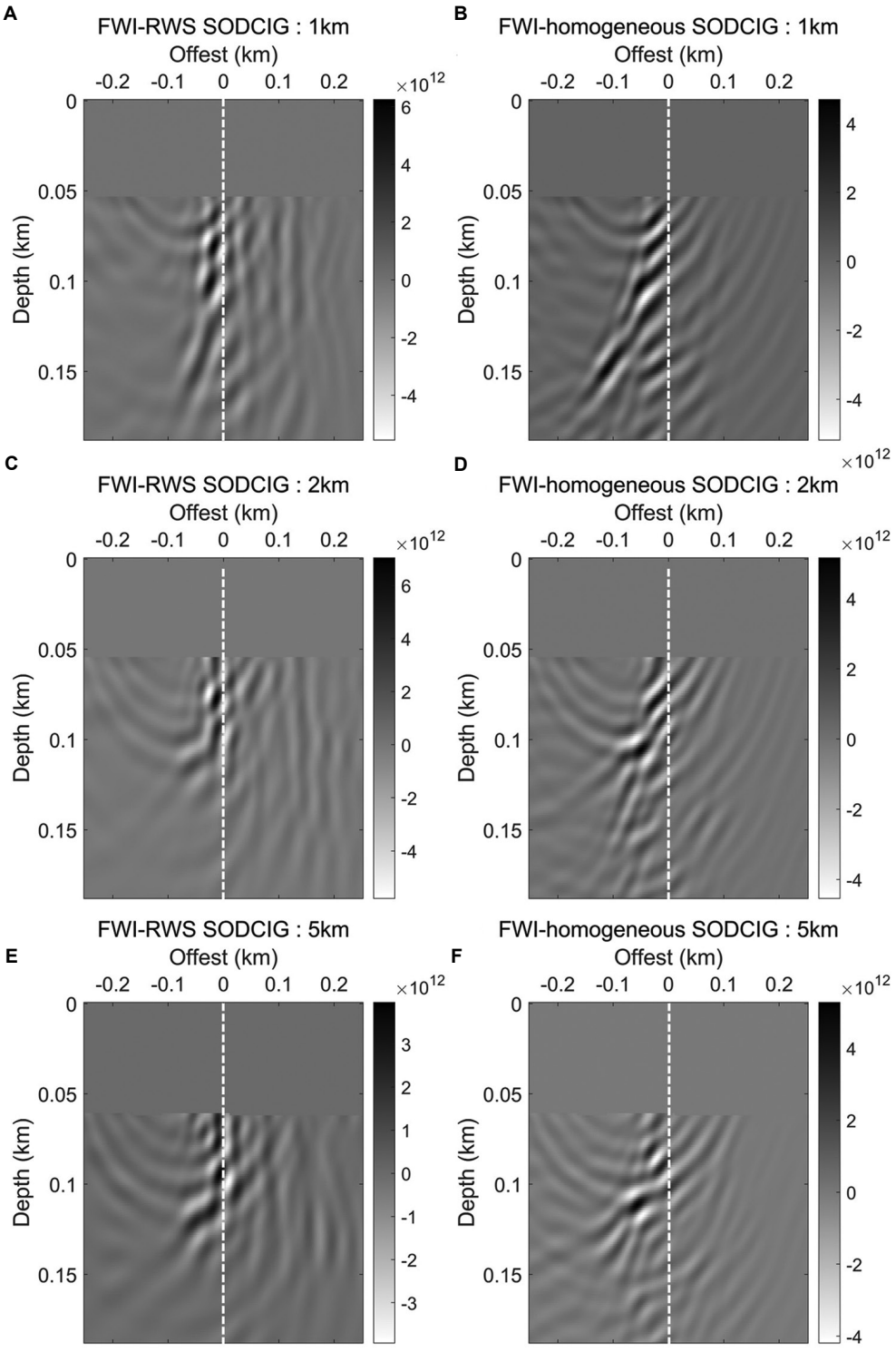

Figure 14. Subsurface offset domain common image gathers at (A and B) 1 km, (C and D) 2 km, and (E and F) 5 km. (A), (C), and (E) are obtained by reverse time migration (RTM) using FWI-RWS results, while (B), (D), and (F) are obtained by RTM using a homogeneous model. The offset range of each common depth point is from −0.2 km to 0.2 km. The white dashed lines mark the common depth point (CDP) location (1 km in [A and B], 2 km in [C and D], and 5 km in [E and F]).

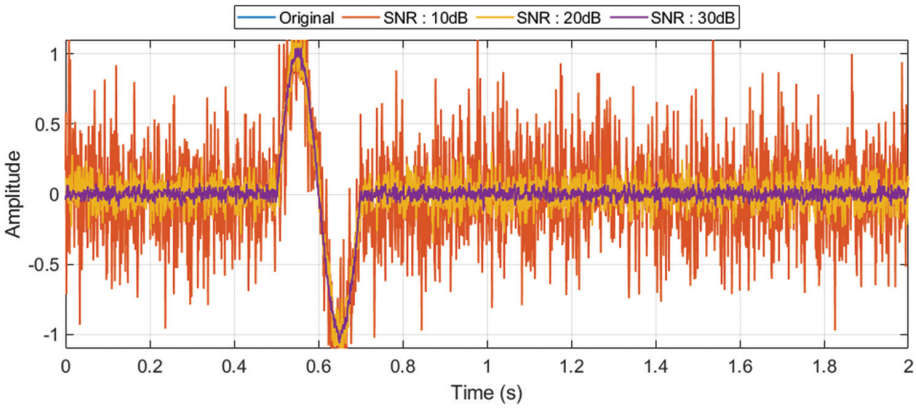

Figure 15. Seismic trace with low signal-to-noise ratio (SNR; 10–30 dB)

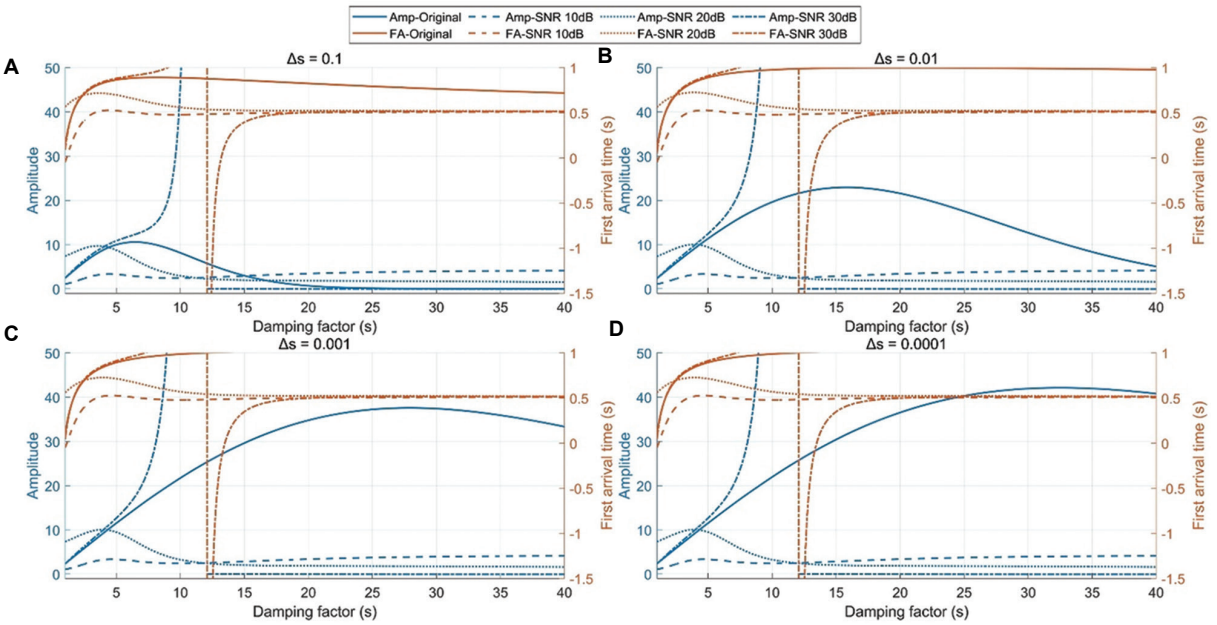

Figure 16. The scenarios with unknown first-arrival traveltime. Variations in the first-arrival traveltime and amplitude in relation to the Laplace damping constant, with a Laplace damping constant interval of (A) 0.1, (B) 0.01, (C) 0.001, or (D) 0.0001.
Abbreviations: Amp: Amplitude; FA: First-arrival traveltime; SNR: Signal-to-noise ratio.

picking is performed for each source, ensuring accurate determination of first-arrival traveltime. At very low SNR levels, our analysis showed that the first-arrival traveltime and amplitude remained consistent across SNRs, provided the first-arrival traveltime of the observed data was accurately known.

5. Conclusion

We presented FWI-RWS, a physics-guided framework that leverages the SWEET method-derived first-arrival traveltime and amplitude. This is achieved by convolving a target source wavelet and gradually increasing its maximum frequency. The potential of the proposed method lies in its ability to enhance resolution incrementally through multi-scale inversion. Both synthetic and field experiments show that FWI-RWS recovers a reliable long-wavelength background from poor initial models and delivers clear RTM focusing improvements when used as the migration velocity model. When applied to field data and used as the background velocity model for RTM, FWI-RWS yields more accurate structural results than a homogeneous velocity model. In addition, we examined the sensitivity of

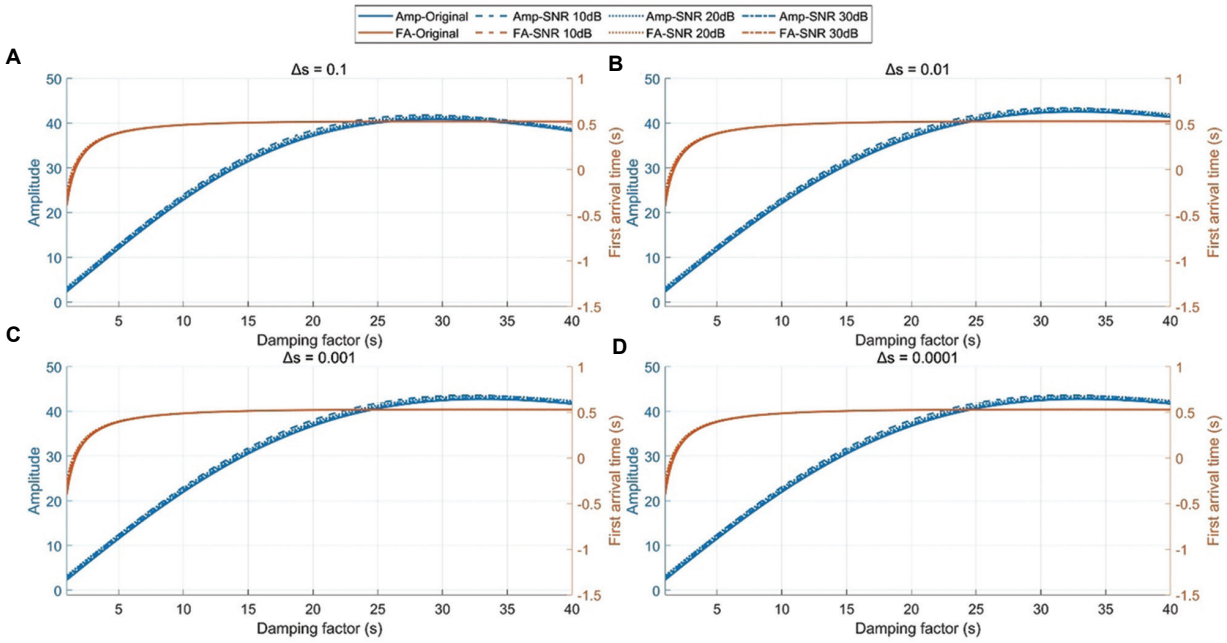

Figure 17. The scenarios with known first-arrival traveltime. Variations in the first-arrival traveltime and amplitude in relation to the Laplace damping constant, with a Laplace damping constant intervals of (A) 0.1, (B) 0.01, (C) 0.001, or (D) 0.0001.
Abbreviations: Amp: Amplitude; FA: First-arrival traveltime; SNR: Signal-to-noise ratio.

the SWEET algorithm to noise, confirming that accurate first-arrival traveltimes and amplitudes can be extracted, provided first-arrival picking is performed beforehand, regardless of noise. Future research will focus on improving the efficiency and applicability of the proposed method by analyzing the impact of different source wavelets and determining the optimal frequency components for the model, with the goal of producing background models that better support attribute analysis, diffraction imaging, and machine learning-based interpretation. Future work will explore adaptive selection of the target-wavelet schedule and extensions to anisotropic and elastic settings.

Acknowledgments

We would like to thank the Korea Institute of Geoscience and Mineral Resources (KIGAM) for permission to publish this work and to show data examples.

Funding

This research was supported by the Korea Institute of Marine Science & Technology Promotion (KIMST), funded by the Ministry of Oceans and Fisheries, Korea (RS-2023-00259633); and the Basic Research Project "Development of operation management infrastructure for TAMHAE 3 and seamless seismic technology connecting coastal areas (25-3322)" of the Korea Institute of Geoscience and Mineral Resources (KIGAM), funded by the Ministry of Science and ICT of Korea.

Conflict of interest

The authors declare that they have no competing interests.

Author contributions

Conceptualization: Seoje Jeong, Wookeen Chung
Formal analysis: Woohyun Son
Funding acquisition: Wookeen Chung
Investigation: Woohyun Son
Methodology: Sumin Kim, Wookeen Chung
Validation: Sumin Kim, Seoje Jeong
Writing–original draft: Seoje Jeong
Writing–review & editing: Seoje Jeong, Wookeen Chung

Availability of data

All data analyzed have been presented in the paper.

References

1. Lailly P, Bednar J. *The Seismic Inverse Problem as a Sequence of Before-Stack Migrations. In: Proceedings SIAM Conference Inverse Scattering*; 1983. p. 206-220.
2. Tarantola A. Inversion of seismic reflection data in the acoustic approximation. *Geophysics*. 1984;49(8):1259-1266. doi: 10.1190/1.1441754

3. Virieux J, Operto S. An overview of full-waveform inversion in exploration geophysics. *Geophysics*. 2009;74(6):WCC1-WCC26.

   doi: 10.1190/1.3238367

4. Mora P. Inversion = migration + tomography. *Geophysics*. 1989;54(12):1575-1586.

   doi: 10.1190/1.1442625

5. Bunks C, Saleck FM, Zaleski S, Chavent G. Multiscale seismic waveform inversion. *Geophysics*. 1995;60(5):1457-1473.

   doi: 10.1190/1.1443880

6. Pratt RG, Shin C, Hicks GJ. Gauss-newton and full newton methods in frequency-space seismic waveform inversion. *Geophys J Int*. 1998;133(2):341-362.

   doi: 10.1046/j.1365-246X.1998.00498.x

7. Gauthier O, Virieux J, Tarantola A. Two-dimensional nonlinear inversion of seismic waveforms: Numerical results. *Geophysics*. 1986;51(7):1387-1403.

   doi: 10.1190/1.1442188

8. Zelt CA, Smith RB. Seismic traveltime inversion for 2-D crustal velocity structure. *Geophys J Int*. 1992;108(1):16-34.

   doi: 10.1111/j.1365-246X.1992.tb00836.x

9. Zhang J, Ten Brink US, Toksöz MN. Nonlinear refraction and reflection travel time tomography. *J Geophys Res Solid Earth*. 1998;103(B12):29743-29757.

   doi: 10.1029/98JB01981

10. Woodward MJ, Nichols D, Zdraveva O, Whitfield P, Johns T. A decade of tomography. *Geophysics*. 2008;73(5):VE5-VE11.

    doi: 10.1190/1.2969907

11. Brenders AJ, Pratt RG. Full waveform tomography for lithospheric imaging: Results from a blind test in a realistic crustal model. *Geophys J Int*. 2007;168(1):133-151.

    doi: 10.1111/j.1365-246X.2006.03156.x

12. Brenders AJ, Pratt RG, Kamei R, Charles S. Waveform Tomography-Marine vs Land: Targets, Challenges and Opportunities. *In: 72nd EAGE Conference and Exhibition-Workshops and Fieldtrips*; 2010. p. 162.

13. Ravaut C, Operto S, Improta L, Virieux J, Herrero A, Dell'Aversana P. Multiscale imaging of complex structures from multifold wide-aperture seismic data by frequency-domain full-waveform tomography: Application to a thrust belt. *Geophys J Int*. 2004;159(3):1032-1056.

    doi: 10.1111/j.1365-246X.2004.02442.x

14. Operto S, Virieux J, Dessa JX, Pascal G. Crustal seismic imaging from multifold ocean-bottom seismometer data by frequency-domain full-waveform tomography: Application to the eastern Nankai Trough. *J Geophys Res Solid Earth*. 2006;111(B9):B09306.

    doi: 10.1029/2005JB003835

15. Bording RP, Gersztenkorn A, Lines LR, Scales JA, Treitel S. Applications of seismic travel-time tomography. *Geophys J Int*. 1987;90(2):285-303.

    doi: 10.1111/j.1365-246X.1987.tb00728.x

16. Moser TJ. Shortest path calculation of seismic rays. *Geophysics*. 1991;56(1):59-67.

    doi: 10.1190/1.1442958

17. Rawlinson N, Sambridge M. Seismic traveltime tomography of the crust and lithosphere. *Adv Geophys*. 2003;46:81-199.

    doi: 10.1016/S0065-2687(03)46002-0

18. Leung S, Qian J. An adjoint-state method for three-dimensional transmission traveltime tomography using first arrivals. *Commun Math Sci*. 2006;4:249-266.

    doi: 10.4310/CMS.2006.v4.n1.a10

19. Liu Y, Wu Z, Geng Z. First-arrival phase-traveltime tomography. *In: SEG 2017 Workshop: Full-Waveform Inversion and Beyond*. United States: SEG; 2017. p. 83-86.

20. Shin C, Cha YH. Waveform inversion in the Laplace domain. *Geophys J Int*. 2008;173(3):922-931.

    doi: 10.1111/j.1365-246X.2008.03768.x

21. Ha W, Pyun S, Yoo J, Shin C. Acoustic full-waveform inversion of synthetic land and marine data in the Laplace domain. *Geophys Prospect*. 2010;58(6):1033-1047.

    doi: 10.1111/j.1365-2478.2010.00884.x

22. Bozdağ E, Trampert J, Tromp J. Misfit functions for full-waveform inversion based on instantaneous phase and envelope measurements. *Geophys J Int*. 2011;185(2):845-870.

    doi: 10.1111/j.1365-246X.2011.04970.x

23. Wu R, Luo J, Wu B. Seismic envelope inversion and modulation-signal model. *Geophysics*. 2014;79(3):WA13-WA24.

    doi: 10.1190/geo2013-0294.1

24. Xiong K, Lumley D, Zhou W. Improved seismic-envelope full-waveform inversion. *Geophysics*. 2023;88(4):R421-R437.

    doi: 10.1190/geo2022-0444.1

25. Xu S, Wang D, Chen F, Lambaré G, Zhang Y. Inversion on reflected seismic wave. *In: SEG Annual International Meeting, Expanded Abstracts*. United States: SEG; 2012. p. 1-7.

    doi: 10.1190/segam2012-1473.1

26. Zhou H, Amundsen L, Zhang G. Fundamental issues in full-waveform inversion. *In: SEG Annual International Meeting, Expanded Abstracts*. United States: SEG; 2012. p. 1-5.

    doi: 10.1190/segam2012-0878.1

27. Berkhout AJ. Combining full wavefield migration and full-waveform inversion: A glance into the future of seismic imaging. *Geophysics*. 2012;77(2):S43-S50.

doi: 10.1190/geo2011-0148.1

28. Dong S, Dong X, Zhang R, Cong Z, Zhong T, Wang H. Global-feature-fusion and multiscale network for low-frequency extrapolation. *IEEE Trans Geosci Remote Sens*. 2024;62:1-14.

doi: 10.1109/TGRS.2024.3408949

29. Operto S, Gholami A, Aghamiry H, Guo G, Beller S. Extending the search space of full-waveform inversion beyond the single-scattering born approximation: A tutorial review. *Geophysics*. 2023;88(6):R671-R702.

doi: 10.1190/geo2022-0758.1

30. Métivier L, Brossier R, Mérigot Q, Oudet E, Virieux J. Measuring the misfit between seismograms using an optimal-transport distance: Application to full-waveform inversion. *Geophys J Int*. 2016;205(1):345-377.

doi: 10.1093/gji/ggw014

31. Van Leeuwen T, Herrmann FJ. Mitigating local minima in full-waveform inversion by expanding the search space. *Geophys J Int*. 2013;195(1):661-667.

doi: 10.1093/gji/ggt258

32. Dong X, Yuan Z, Lin J, Dong S, Tong X, Li Y. *PreAdaptFWI: Pretrained-Based Adaptive Residual Learning for full-Waveform Inversion without Dataset Dependency*. [Preprint]; 2025.

doi: 10.48550/arXiv.2502.11913

33. Muller AP, Costa JC, Bom CR, *et al*. Deep pre-trained FWI: Where supervised learning meets physics-informed neural networks. *Geophys J Int*. 2023;235(1):119-134.

doi: 10.1093/gji/ggad215

34. Cheng S, Wang Y, Zhang Q, Harsuko R, Alkhalifah T. A self-supervised learning framework for seismic low-frequency extrapolation. *J Geophys Res Mach Learn Comput*. 2024;1(3):e2024JH000157.

doi: 10.1029/2024JH000157

35. Wu RS, Toksöz MN. Diffraction tomography and multisource holography applied to seismic imaging. *Geophysics*. 1987;52(1):11-25.

doi: 10.1190/1.1442237

36. Shin C, Min DJ, Lim HY, *et al*. Traveltime and amplitude calculations using the damped-wave solution. *Geophysics*. 2002;67(5):1637-1647.

doi: 10.1190/1.1512811

37. Shin C, Min DJ. Waveform inversion using a logarithmic wavefield. *Geophysics*. 2006;71(3):R31-R42.

doi: 10.1190/1.2194523

38. Shin C, Jang S, Min DJ. Improved amplitude preservation for prestack depth migration by inverse scattering theory. *Geophys Prospect*. 2001;49(5):592-606.

doi: 10.1046/j.1365-2478.2001.00279.x

39. Boonyasiriwat C, Valasek P, Routh P, Zhu X. Application of multiscale waveform tomography for high-resolution velocity estimation in complex geologic environments: Canadian Foothills synthetic-data example. *Lead Edge*. 2009;28(4):454-456.

doi: 10.1190/1.3112764

40. Pasalic D, McGarry R. Convolutional perfectly matched layer for isotropic and anisotropic acoustic wave equations. *In: SEG International Exposition and Annual Meeting*. United States: SEG; 2010.

doi: 10.1190/1.3513453

41. Aminzadeh F, Burkhard N, Nicoletis L, Rocca F, Wyatt K. SEG/EAEG 3-D modeling project: Second update. *Lead Edge*. 1994;13(9):949-952.

doi: 10.1190/1.1437054

42. Symes WW. A differential semblance criterion for inversion of multioffset seismic reflection data. *J Geophys Res*. 1993;98(B2):2061-2073.

doi: 10.1029/92JB01304

43. Prucha ML, Biondi BL, Symes WW. Angle-domain common-image gathers by wave-equation migration. *In: SEG Technical Program Expanded Abstracts*. United States: SEG; 1999. p. 824-827.

doi: 10.1190/1.1821156

44. Xu S, Chauris H, Lambaré G, Noble M. Common-angle migration: A strategy for imaging complex media. *Geophysics*. 2001;66(6):1877-1894.

doi: 10.1190/1.1487131

45. Zhou H, Gray SH, Young J, Pham D, Zhang Y. Tomographic residual curvature analysis: The process and its components. *In: SEG Technical Program Expanded Abstracts*. United States: SEG; 2003. p. 666-669.

doi: 10.1190/1.1818018

46. Sava PC, Fomel S. Angle-domain common-image gathers by wavefield-continuation methods. *Geophysics*. 2003;68(3):1065-1074.

doi: 10.1190/1.1581078

47. Valenciano AA, Biondi B. Wave-equation angle-domain Hessian. *In: 68th EAGE Conference and Exhibition Incorporating SPE EUROPEC*. 2006. p. 2.

doi: 10.3997/2214-4609.201402166

48. Chauris H, Lameloise CA, Donno D. Migration velocity analysis with reflected and transmitted waves. In: *75th EAGE Conference and Exhibition Incorporating SPE EUROPEC*. 2013. p. 348.

doi: 10.3997/2214-4609.20130936

49. Kalita M, Alkhalifah T. Common-image gathers using the excitation-amplitude imaging condition. *Geophysics*. 2016;81(4):S261-S269.

doi: 10.1190/geo2015-0413.1